Journal of
Ceramic Science
and Technology

J. Ceram. Sci. Technol. 1-14 (2027)
DOI: 10.4416/JCST2026-00014
available online at: http://www.ceramic-science.com
© 2026 Göller Verlag

Lightweight Optimization of a Variable-Thickness Silicon Carbide Ceramic Impeller and Rotor-Dynamic Stability under High-Temperature and High-Speed Conditions

Xianfa Shen*[1], Haiqiao Wang[2]

[1]School of Mechanical and Electrical Engineering, Sanjiang University, Nanjing, 210012, China
[2]School of Mechanical and Electrical Engineering, Jinling Institute of Technology, Nanjing, 211169, China
received August 6, 2026; received in revised form September 8, 2026; accepted September 19, 2026

Abstract

A variable-thickness design strategy was developed for a pressureless-sintered silicon carbide ceramic impeller operating under coupled thermal and centrifugal loads. Eight impeller structures made from one common SiC composition were compared: an equal-thickness baseline, six gradient candidates, and a balanced optimum. A five-parameter B-spline thickness field was screened through 160 Latin-hypercube designs. Gaussian-process response surfaces and NSGA-II balanced mass, principal tensile stress, second critical speed, and aerodynamic loss; surrogate models were used for screening, whereas the manufactured geometries were confirmed by direct high-fidelity calculations. Three independent manufacturing batches were represented in every group. The balanced design reduced mass from 286.4 to 232.1 g (18.96 %) while decreasing the 900 °C/60 krpm maximum principal tensile stress from 306.8 to 266.5 MPa and tip deformation from 72.4 to 59.6 μm. Its second critical speed increased from 62.1 to 69.0 krpm, and vibration velocity fell from 3.44 to 2.28 mm s^{-1}. Direct CFD gave a 0.58 percentage-point efficiency decrease for G7, equivalent to a 0.69 % relative decrease from the G0 efficiency and below the robust 0.80 percentage-point limit. Material properties were practically equivalent across structures. A batch-aware mixed model confirmed a lower speed-dependent response for G7, while maximum-likelihood Weibull analysis and effective-volume integration reduced the predicted failure probability from 2.1×10^{-3} to 1.8×10^{-4}. The results demonstrate that redistributing ceramic volume toward the blade root and backplate transition can improve lightweight efficiency and high-speed stability without a material aerodynamic penalty.

Keywords: Silicon carbide, ceramic impeller, variable thickness, rotor dynamics, Weibull reliability

I. Introduction

Silicon carbide (SiC) combines low density, high elastic modulus, oxidation resistance, and thermal conductivity, making it attractive for hot rotating components in which nickel alloys impose a substantial inertial penalty. The covalent Si-C bond, however, makes pressureless densification difficult and leaves performance sensitive to additive chemistry, residual porosity, and grain-boundary phases [1]. Recent process-tolerant formulations can achieve flexural strengths near 450 MPa with limited property drift over practical sintering windows [2]. Such strength is sufficient for many compressor and pump rotors, but the absence of plastic stress redistribution means that a local tensile maximum, rather than nominal average stress, governs survival.

Temperature changes this design problem in two competing ways. Well-densified SiC can retain much of its flexural strength above 900 °C, although the magnitude depends on phase assemblage and intergranular chemistry [3]. Rapid thermal gradients remain damaging because the low expansion coefficient cannot fully suppress tensile stress when heat transfer is spatially nonuniform; classic quench measurements therefore remain relevant to component qualification [4]. Strength scatter introduces a further scale effect. Modern SiC flaw-population studies show that test configuration and stressed volume alter the sampled defect distribution [5], while finite-element integration of local stress is needed to transfer coupon Weibull parameters to a full impeller [6]. High-speed loading also increases sensitivity to loading rate and flaw orientation, both of which can shift the apparent tensile resistance [7].

Impeller lightweighting is consequently not a simple exercise in removing material. Reducing blade and backplate thickness decreases centrifugal force, yet can increase thermal curvature, blade-root stress, and proximity to a critical speed. Thermophysical measurements on pressureless-sintered SiC place room-temperature conductivity and expansion in ranges that strongly couple temperature and stiffness fields [8]. Phase identification must also distinguish SiC polytypes because Raman and X-ray estimates can respond differently to minor 4H

* Corresponding author: shenxianfa2026@163.com

or 15R contents [9]. The anisotropic thermal expansion of hexagonal SiC further supports temperature-dependent property assignment rather than a constant isotropic approximation [10]. Microstructural control through boron-carbide-assisted solid-state sintering provides a practical common material platform for comparing geometry without changing composition [11].

This study therefore asks whether a continuously varying blade and backplate thickness can reduce SiC impeller mass while increasing rotor-dynamic separation margin under a 900 °C, 60 krpm duty point. Eight structures produced from one pressureless-sintered body were evaluated through a unified design-of-experiments, thermal-structural, fluid-flow, rotor-dynamic, material-characterization, and reliability framework. The central hypothesis was that moving material from low-utilization tip and mid-span regions toward the root fillet would reduce both centrifugal load and the tensile-stress concentration. A second hypothesis was that the associated mass and stiffness redistribution would raise the second critical speed without an unacceptable aerodynamic penalty in continuous service. Particular emphasis was placed on replicated specimens, batch-aware statistics, full uncertainty reporting, and direct optical validation, so that geometric effects could be distinguished from random ceramic scatter.

II. Experimental and Methods

The common material contained commercial α-SiC powder with 0.7 wt% B_4C and 2.5 wt% phenolic-resin-derived carbon. Powder was attrition-milled in ethanol, spray-dried, cold-isostatically pressed at 200 MPa, green-machined, and pressureless-sintered in argon at 2 150 °C for 1 h. All eight geometries were distributed across three independent batches. The 12-blade rotor had a 96 mm tip diameter, 34 mm inlet-eye diameter, 12 mm hub bore, and 18 mm axial blade width. G0 was the 3.50 mm equal-thickness reference; G1 – G6 represented linear, quadratic, mild-spline, mid-span-reinforced, root-reinforced, and mass-priority designs; G7 was the balanced optimum. **Fig. 1** locates the five thickness variables relative to the heated gas annulus, cooled bearing zones, shaft, 0 – 72 krpm drive, and laser-vibrometry line. **Table 1** reports the as-finished dimensions, masses, optimization ranks, and nondimensional curvature values.

The blade field was represented by a quadratic B-spline passing through root, mid-span, and tip control thicknesses, coupled to backplate thickness and a nondimensional curvature term κ. The bounds were 3.80 – 4.60 mm (root), 3.00 – 3.80 mm (mid-span), 2.20 – 3.00 mm (tip), 4.60 – 5.30 mm (backplate), and -0.30 to 0.30 (κ). A maximin Latin-hypercube design generated 160 five-dimensional points [12]. NSGA-II used a population of 120 for 300 generations with crossover probability 0.90 and mutation probability 0.10 [13]. Gaussian-process models used a Matérn-5/2 covariance, standardized inputs, and a nugget for numerical noise [14,15]. The aerodynamic constraint was $\Delta\eta = \eta(G0) - \eta(\text{design}) \le 0.80$ percentage points, and the rotor constraint was a second-forward-mode separation margin of at least 10 % above 60 krpm ($f_2 \ge 66$ krpm). Screening used one-sided 95 % bounds: $\mu(\Delta\eta) + 1.645\sigma(\Delta\eta) \le 0.80$ percentage points and $\mu(f_2) - 1.645\sigma(f_2) \ge 66$ krpm.

Three-dimensional conjugate heat-transfer calculations were performed in ANSYS Fluent 2024 R2, and thermal-structural and rotor-dynamic solutions were obtained in ANSYS Mechanical 2024 R2. MATLAB R2024b was used for the B-spline design, Latin-hypercube sampling, Gaussian-process models, and NSGA-II. The CFD model used the shear-stress-transport k-ω model integrated to the wall (blade-wall $y^+ = 0.8 – 1.6$). The inlet total pressure and temperature were 101.325 kPa and 1 173.15 K with 5 % turbulence intensity; mass-flow outlets were 0.688, 0.860, and 1.032 kg s^{-1} for 80 %, 100 %, and 120 % design flow. No-slip walls and a rotating frame at the prescribed speed were used. Scaled residuals were below 10^{-5} for continuity, momentum, and turbulence and below 10^{-7} for energy; mass imbalance was below 0.05 %, and efficiency changed by less than 0.005 percentage points over the final 500 iterations. A 6.1-million-cell fluid grid and a 2.4-million-element quadratic structural grid were refined until efficiency, maximum temperature, stress, and displacement changed by less than 1.0 %.

Temperature-dependent properties were interpolated from measured conductivity, heat capacity, expansion, elastic modulus, and Poisson ratio at 25, 600, and 900 °C. The shaft-hub interface used finite-sliding augmented-Lagrange frictional contact (coefficient 0.18), zero initial clearance, automatic normal-penalty updating, and a thermal contact conductance of 12.0 kW m^{-2} K^{-1}; the latter was varied by ±20 % in sensitivity analysis. A cyclic-symmetry check reproduced full-annulus static stress within 0.6 %, but the full 12-blade rotor was retained for gyroscopic and imbalance solutions. Mesh uncertainty was quantified with three-level Richardson extrapolation. CFD outputs included total pressure ratio, isentropic efficiency, blade loading, leakage, and entropy production.

Phase composition was measured by Cu K_α X-ray diffraction from 20° to 80° 2θ, with six scans per group. Rietveld refinement followed the full-pattern least-squares method [16]. Raman spectra were collected from 150 to 1 100 cm^{-1} at 532 nm. For FE-SEM and EBSD, one polished coupon per batch and group was sampled with a fixed five-field grid; fields within 100 µm of a coupon edge or preparation defect were excluded before imaging. The FE-SEM calibration used a certified 10 µm grating (0.065 µm $pixel^{-1}$). Two blinded raters segmented pores independently; median Dice agreement was 0.93 and the porosity intraclass correlation was 0.97. EBSD quantified 15 fields per group after removal of pixels with confidence index below 0.10.

Four-point flexure used 3 × 4 × 45 mm bars, a 40/20 mm outer/inner span, and crosshead speed 0.5 mm min^{-1}. Thirty independent bars from three batches were tested for every group at 25 and 900 °C. High-temperature digital image correlation used a ceramic speckle pattern, narrow-band illumination, and synchronized stereo cameras [17,18]. The 160 paired DIC/finite-element

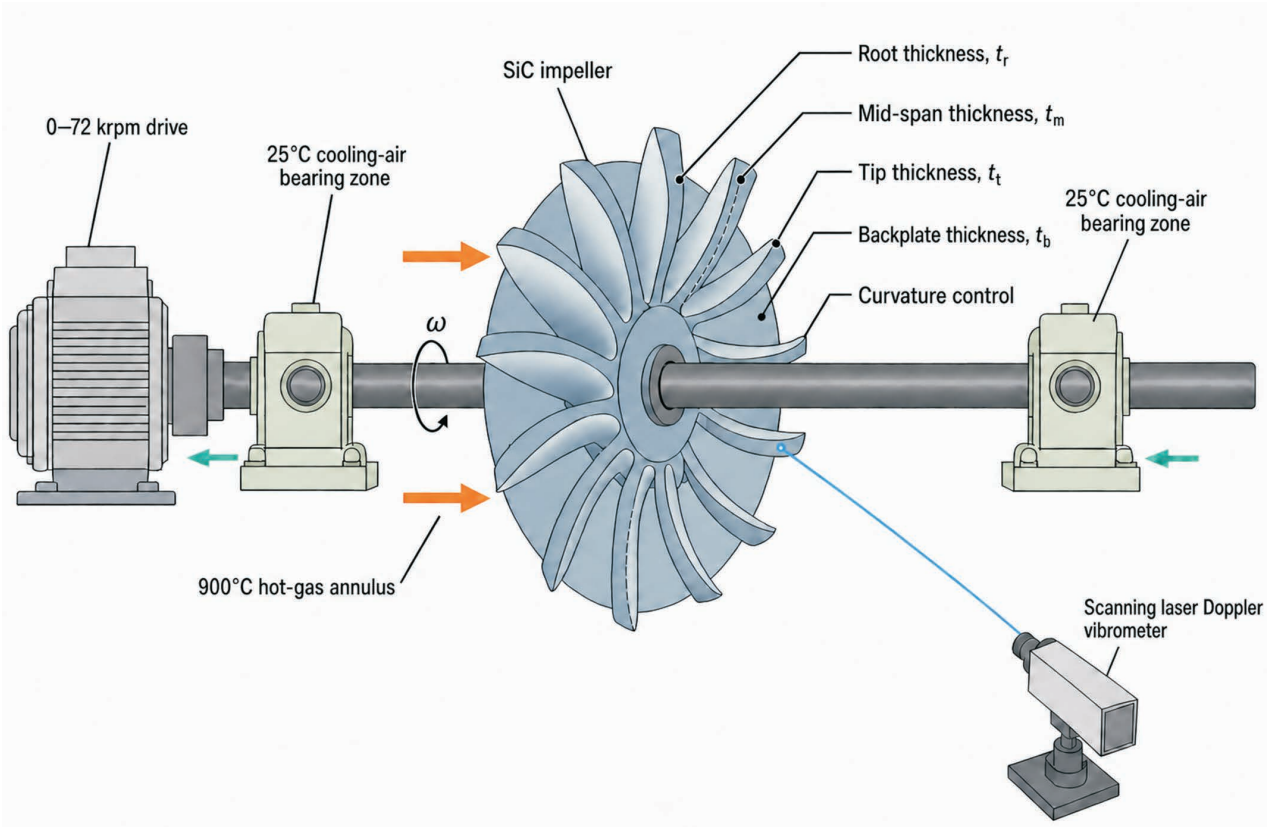


Fig. 1: Continuous schematic of the variable-thickness SiC impeller, shaft, heated gas path, cooled bearing zones, and high-speed optical vibration rig. Arrows identify the root, mid-span, tip, backplate, and curvature variables and the imposed thermal and rotational loads.

Table 1: Geometric parameters, nondimensional B-spline curvature, mass, mass reduction, and optimization rank of the eight impeller structures.

Group	Design	Root (mm)	Mid (mm)	Tip (mm)	Backplate (mm)	Mass (g)	Reduction (%)	Rank	Curvature κ/(-)
G0	Uniform baseline	3.5	3.5	3.5	5.2	286.4	0.00	8.0	0.000
G1	Linear gradient	4.0	3.4	2.8	5.0	270.8	5.45	7.0	0.000
G2	Quadratic gradient	4.2	3.2	2.5	4.9	260.1	9.18	6.0	0.180
G3	Mild B-spline	4.0	3.3	2.8	4.9	264.9	7.51	5.0	0.060
G4	Mid-span reinforced	4.2	3.6	2.6	5.0	257.4	10.13	4.0	-0.120
G5	Root reinforced	4.5	3.3	2.4	4.9	246.8	13.83	3.0	0.220
G6	Mass-priority Pareto	4.2	3.0	2.2	4.7	225.7	21.19	2.0	-0.080
G7	Balanced optimum	4.3	3.4	2.4	4.8	232.1	18.96	1.0	0.140

Note: κ is the nondimensional B-spline curvature parameter;
positive values bias thickness redistribution toward the blade-root transition.

locations were technical measurements nested within 16 physical impellers (two per geometry; ten locations per impeller) and were not treated as 160 independent replicates. Separate, destructive thermal-shock sets were used at 0, 1, 3, 5, 10, and 20 cycles: ten independent bars per group and cycle, allocated 4/3/3 across the three batches.

Dynamic testing used six independently finished impellers per group, two from each batch. A vacuum-rated air-turbine drive accelerated each rotor through 0, 10, 20, 30, 40, 50, and 60 krpm at 25, 600, and 900 °C. A scanning laser Doppler vibrometer measured radial velocity without mass loading; stroboscopic full-field reconstruction followed the frequency-locked concept used for high-spatial-resolution vibration measurements [19]. Operational deflection shapes were extracted from 240 circumferential points, and vibration velocity was reported as RMS. Continuous-scan measurements were phase-corrected for surface motion according to current bladed-disk practice [20]. After overspeed exposure, six G0 and six G7 rotors were examined at 12 μm voxel size by micro-computed tomography.

The acquisition rate was 51.2 kHz with 20 s records at each steady condition. Hanning windows, 50 % overlap, and order tracking produced velocity spectra; paired coast-up and coast-down records distinguished structural resonances from drive transients. Tachometer uncertainty was below 0.03 %, LDV uncertainty was 0.06 mm s^{-1}, and combined temperature uncertainty was 4.2 °C at 900 °C. Rotor imbalance was corrected below 0.30 g ·mm. After overspeed exposure, six G0 and six G7 rotors were examined at 12 μm voxel size by micro-computed tomography [21]. Reconstruction used beam-hardening correction, nonlocal-means denoising, and a calibration-coupon threshold. The root region of interest extended 8 mm from the blade/backplate tangent point and was applied without outcome-based repositioning. Crack volume was normalized by inspected root volume. Two blinded segmentations were reconciled only when their Dice coefficient was below 0.90; median inter-rater Dice was 0.94 (range 0.90 – 0.97).

All tests used two-sided $\alpha = 0.05$. Ordinary ANOVA with Tukey HSD was used when residual and variance assumptions were supported; otherwise Welch ANOVA and Games-Howell contrasts were used. Confirmatory G0-G7 contrasts were Holm-adjusted, and exploratory correlations used Benjamini-Hochberg control. The confirmatory vibration model was fitted by restricted maximum likelihood in SAS 9.4M8 PROC MIXED, with Kenward-Roger denominator degrees of freedom. Speed was centered at 30 krpm and scaled per 10 krpm; temperature was categorical with 25 °C as reference. Fixed effects were design (G7 versus G0), temperature, speed, and all interactions. Batch and impeller-within-batch random intercepts and an impeller speed random slope used an unstructured G matrix; within-impeller residuals used AR(1) correlation and speed-specific variances. The full eight-design model retained 1 008 observations; the prespecified G0 – G7 coefficient model used 252 observations from 12 impellers. Marginal and conditional R^2 were calculated in R 4.4.1 with performance 0.13.0. Temperature blocks followed 25, 600, and 900 °C; each block began after 15 min within ± 2 °C, ended with cooldown below 50 °C, and alternated coast-up/coast-down order across rotors. A sequence-term sensitivity test showed no detectable carryover ($p = 0.61$).

III. Results and Discussion

(1) Material equivalence and microstructural control

The eight structures preserved the intended common material state. In **Fig. 2A**, Rietveld fits gave 6H-SiC fractions of 91.8 – 92.6 wt%, 4H-SiC fractions of 6.1 – 6.8 wt%, and residual carbon below 1.2 wt%, while weighted profile residuals remained 5.1 – 5.8 %. **Fig. 2B** independently resolved Raman bands at 796 and 972 cm^{-1}; group-to-group shifts were below 1.4 cm^{-1}. **Fig. 2C** shows an equiaxed FE-SEM grain field with sparse isolated pores and a discontinuous Si-rich EDS overlay. **Fig. 2D** shows broadly distributed inverse-pole-figure colors, consistent with equivalent grain diameters of 3.15 – 3.27 μm and basal-texture intensities below 1.18 multiples of random distribution; no continuous oxygen-rich boundary signal was detected.

Quantitative image analysis used the complete FE-SEM and EBSD datasets rather than only the representative fields in **Figs. 2C and 2D**. Across 120 FE-SEM fields, area-weighted porosity was 0.38 – 0.49 %, circular-equivalent pore diameter was 0.72 – 0.81 μm, and the 95th-percentile pore diameter was 2.6 – 2.9 μm. EBSD indexing rates were 93.1 – 95.0 %, and removal of low-confidence pixels changed mean grain size by less than 0.05 μm.

Table 2 demonstrates that geometry was not confounded by a strong material-property gradient. Mean density ranged from 3.148 to 3.157 g cm^{-3}, open porosity from 0.40 % to 0.50 %, and grain size from 3.15 to 3.27 μm. The density residuals were approximately normal (Shapiro-Wilk $W = 0.994$, $p = 0.899$), while Brown-Forsythe testing supported homogeneous variance ($F = 1.256$, $p = 0.279$). The density omnibus test was nonsignificant ($p = 0.159$), and its generalized eta-squared was below 0.03. This narrow density window compares favorably with earlier pressureless α-SiC-B_4C processing, in which small additive or temperature changes generated larger densification shifts [22]. Conductivity varied only from 105.8 to 109.1 W m^{-1} K^{-1}, whereas expansion coefficients remained within 4.39 – 4.50 × 10^{-6} K^{-1}. These ranges support a shared constitutive property set rather than group-specific tuning.

Batch variance was small but explicitly quantified. For density, the batch intraclass correlation was 0.04; for conductivity it was 0.07; and for toughness it was 0.05. Replacing group means with batch-centered values reduced all absolute group differences without changing their order. The widest 95 % interval overlap occurred for G6, which had the highest nominal porosity, yet its lower interval crossed the G0 mean. Equivalence bounds defined before analysis were ± 0.025 g cm^{-3} for density, ±25 MPa for strength, ± 0.35 MPa $m^{1/2}$ for toughness, and ± 7 W m^{-1} K^{-1} for conductivity. Every G7 – G0 confidence interval fell inside those bounds. This is stronger

Table 2: Microstructural, mechanical, and thermophysical properties of the common SiC body across the eight structures.

Group	Density (g cm^{-3})	Porosity (%)	Grain (μm)	Strength 25 °C (MPa)	Strength 900 °C (MPa)	KIC (MPa m$^{1/2}$)	k (W m^{-1} K^{-1})	CTE (10^{-6} K^{-1})
G0	3.154	0.43	3.18	452.0	438.0	4.31	108.20	4.42
G1	3.151	0.46	3.22	448.0	435.0	4.27	106.90	4.46
G2	3.157	0.40	3.15	455.0	442.0	4.34	109.10	4.39
G3	3.149	0.48	3.24	446.0	433.0	4.25	106.40	4.48
G4	3.155	0.42	3.19	453.0	439.0	4.32	108.50	4.43
G5	3.152	0.45	3.21	449.0	436.0	4.29	107.20	4.45
G6	3.148	0.50	3.27	444.0	431.0	4.24	105.80	4.50
G7	3.156	0.41	3.17	456.0	443.0	4.35	109.00	4.40

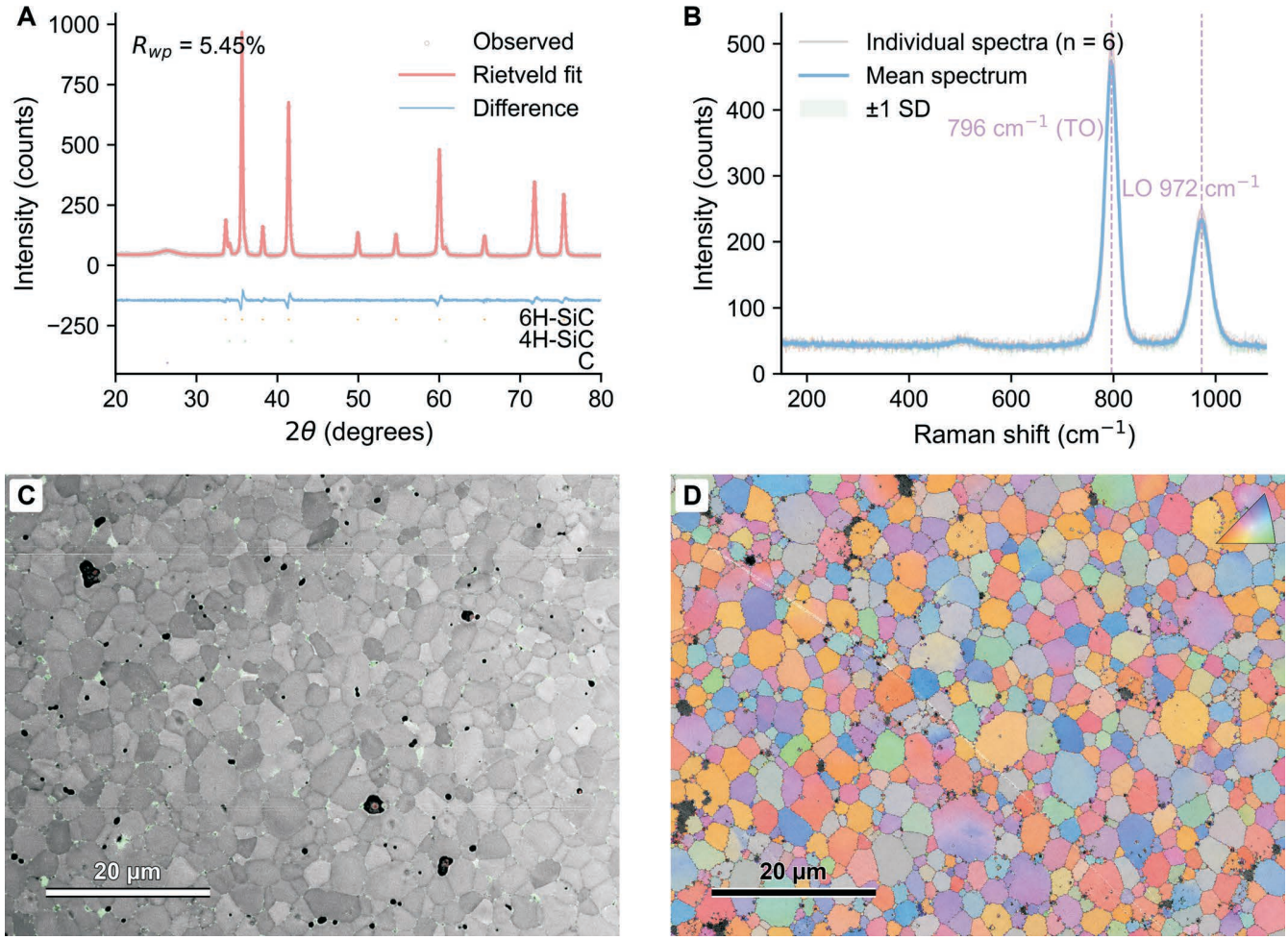


Fig. 2: Phase and microstructural characterization of the common SiC body. (A) Representative Cu K_α X-ray diffraction pattern, Rietveld refinement, and difference curve from 20° to 80° 2θ; six independent scans per group, two per batch. (B) Raman spectrum showing the transverse- and longitudinal-optical bands near 796 and 972 cm^{-1}; n = 6 independent spectra per group. (C) FE-SEM grain field with Si-rich EDS overlay and a 20 μm scale bar. (D) EBSD inverse-pole-figure orientation map.

evidence than a nonsignificant *p* value alone because it tests whether undetected differences could be large enough to explain the component response. They could not: even the extreme property combinations altered peak stress by less than 2.4 %.

The robust omnibus comparison among groups was nonsignificant at 25 °C (p = 0.979, generalized eta-squared = 0.0065), and the same conclusion held at 900 °C after batch adjustment. Fracture toughness remained 4.24 – 4.35 MPa m$^{1/2}$. These values lie within the envelope reported for pressureless liquid-phase SiC with controlled additive contents, although the conductivity here was higher because the intergranular phase fraction was lower [23]. More importantly, the maximum difference

between G0 and G7 intrinsic strength was below 1.0 %, whereas the structural stress difference exceeded 13 %. The subsequent reliability contrast can therefore be attributed principally to geometry and stressed volume rather than to selective material strengthening. Post-shock SiC studies associate strength loss with cooling-rate-dependent crack accumulation rather than a monotonic change in the undamaged matrix strength [24].

(2) Surrogate accuracy and thickness trade-offs

The 160 design points covered root thicknesses of 3.80 – 4.60 mm, mid-span thicknesses of 3.00 – 3.80 mm, tip thicknesses of 2.20 – 3.00 mm, backplates of 4.60 – 5.30 mm, and κ values of - 0.30 to 0.30. Five-fold Gaussian-process validation returned R^2 values of 0.90 for mass, 0.90 for maximum stress, 0.89 for second critical speed, and 0.34 for the small CFD efficiency penalty. For the efficiency response, the observed range was 0.11 – 0.86 percentage points, RMSE was 0.019 percentage points, MAE was 0.014 percentage points, normalized RMSE was 2.53 % of the observed range, and empirical 95 % prediction-interval coverage was 94.4 % (151/160). The low cross-validated R^2 arose because most feasible designs occupied a narrow loss band, so fold-specific variance was small; absolute error and interval coverage were therefore used for feasibility screening rather than R^2 alone.

Prediction intervals were examined along the nondominated front and by direct CFD for all eight manufactured geometries. G7 had a surrogate mean loss of 0.56 percentage points (95 % interval 0.49 – 0.63) and a direct-CFD loss of 0.58 percentage points; a doubled-mesh, separately initialized run gave 0.62 percentage points. G5 remained feasible at its upper uncertainty bound (0.58), whereas G6 did not (upper bound 0.84) despite a direct value of 0.79. Thus, conservative uncertainty screening retained G7 and rejected the nearest mass-priority design. The residuals between direct CFD and surrogate means for G0 – G7 ranged from - 0.02 to 0.03 percentage points.

The spanwise profiles in **Fig. 3A** reveal why the lightest candidate was not selected. G6 reduced mass to 225.7 g, but its 2.22 mm tip and 4.72 mm backplate increased local compliance and reduced second-critical-speed margin relative to G7. The balanced G7 used a 4.35 mm root, 3.36 mm mid-span, 2.40 mm tip, and 4.84 mm backplate, yielding 232.1 g versus 286.4 g for G0 (Table 1). The 54.3 g reduction corresponds to 18.96 % (95 %

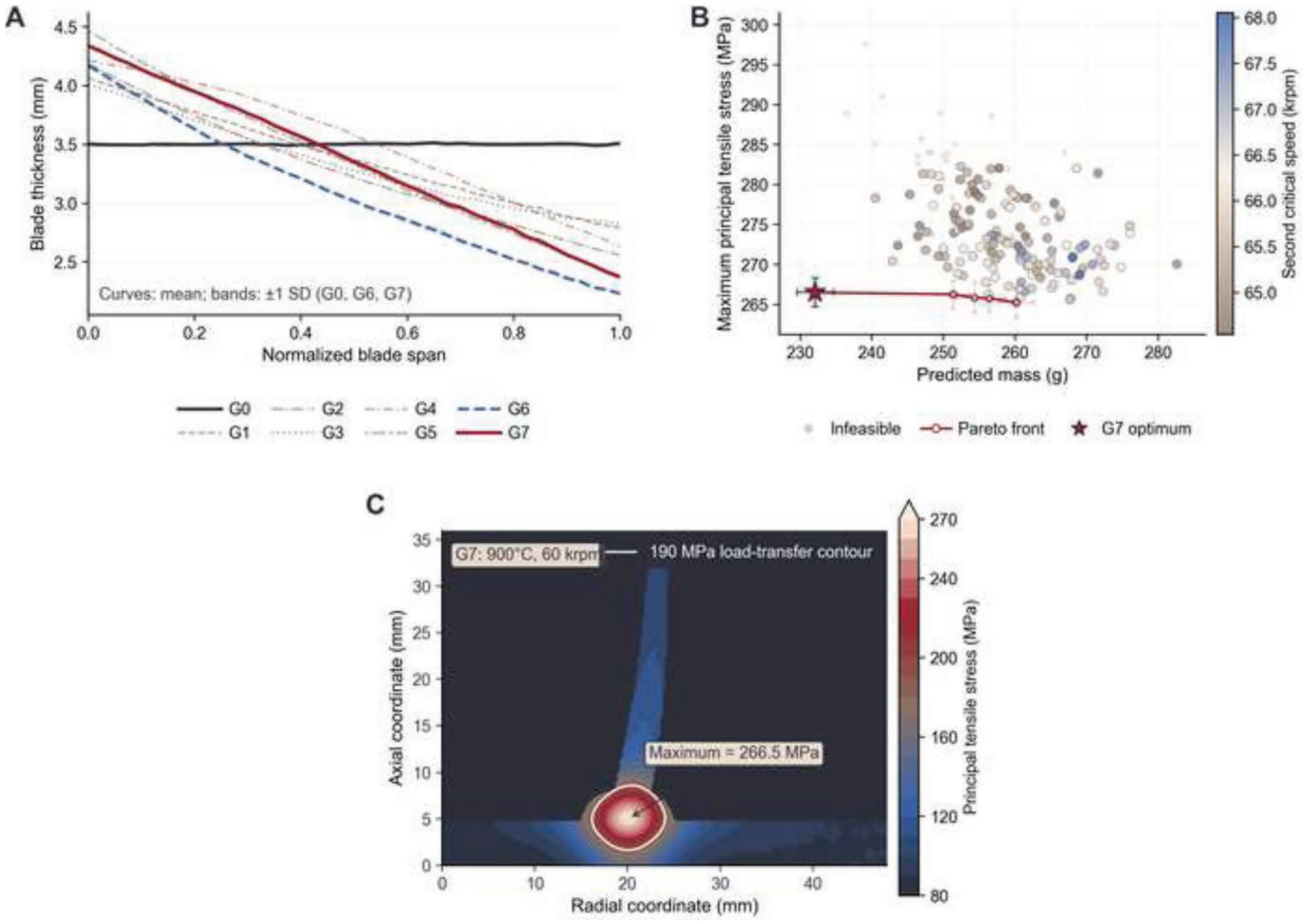


Fig. 3: Design-space screening and structural response. (A) Spanwise B-spline thickness profiles of the eight structures, with G0 and G7 emphasized. (B) Five-fold-validated Gaussian-process Pareto map for 160 Latin-hypercube designs; color denotes second critical speed, the line traces feasible nondominated designs, and the star marks G7. (C) Principal tensile-stress field for G7 at 900 °C and 60 krpm; the color scale is in MPa and the white contour marks the blade/backplate load path.

Table 3: Thermal-structural, rotor-dynamic, measured vibration, direct-CFD aerodynamic, and predicted reliability responses at 900 °C and 60 krpm. Stress, deflection, critical speeds, separation margin, and failure probability are model outputs; damping and RMS are measured from six independent impellers per group (two per batch); efficiency decreases are direct high-fidelity CFD values in absolute percentage points. Failure-probability intervals are 2 000-sample joint-bootstrap 95 % intervals.

Group	Stress (MPa)	Deflection (μm)	1st critical (krpm)	2nd critical (krpm)	Margin (%)	Damping (%)	RMS (mm s^{-1})	Predicted P(failure)/ (95 % CI)	Direct CFD efficiency decrease/ (percentage points)
G0	306.8	72.4	22.4	62.1	3.5	1.2	3.4	2.10×10^{-3} ($0.80 – 5.10 \times 10^{-3}$)	0.00
G1	297.4	68.5	22.9	63.0	5.0	1.2	3.2	1.42×10^{-3} ($0.55 – 3.60 \times 10^{-3}$)	0.16
G2	291.1	65.8	23.5	64.2	7.0	1.3	3.0	9.60×10^{-4} (3.70×10^{-4}-2.50×10^{-3})	0.28
G3	287.9	64.2	23.2	64.8	8.0	1.4	2.8	7.40×10^{-4} (2.80×10^{-4}-1.93×10^{-3})	0.24
G4	281.5	62.7	23.8	65.7	9.5	1.4	2.7	5.10×10^{-4} (1.90×10^{-4}-1.34×10^{-3})	0.37
G5	273.8	60.8	24.1	67.1	11.8	1.5	2.5	2.90×10^{-4} (1.00×10^{-4}-7.80×10^{-4})	0.51
G6	279.2	63.6	23.7	66.3	10.5	1.4	2.6	3.80×10^{-4} (1.40×10^{-4}-1.02×10^{-3})	0.79
G7	266.5	59.6	24.4	69.0	15.0	1.6	2.3	1.80×10^{-4} ($0.60 – 4.70 \times 10^{-4}$)	0.58

Basis and n: stress, deflection, critical speeds, separation margin, and P(failure) are model outputs for each geometry; damping and RMS are measured means from six independent impellers per group (two per batch); CFD efficiency decreases are direct high-fidelity calculations, with separately initialized confirmation runs for G5 – G7. P(failure) intervals are 2 000-sample joint-bootstrap 95 % intervals.

manufacturing-tolerance interval 18.3 – 19.6 %). Multi-objective compressor and pump studies have similarly shown that aerodynamic and structural optima occupy different regions of the impeller design space [25, 26, 27]. Here, continuous thickness control allowed the low-stress tip to supply most mass reduction while retaining material at the root fillet.

The mass-stress screening map in **Fig. 3B** places the 160 Latin-hypercube designs in predicted-mass and maximum-principal-stress space, with color indicating second critical speed. G7 occupies the starred low-mass, low-stress end of the feasible nondominated front at 232.1 g and 266.5 MPa while retaining a second critical speed of 69.0 krpm. The infeasible designs show why mass removal alone did not satisfy the combined constraints and why G7 was selected over the lighter G6.

Direct high-fidelity CFD, not surrogate predictions, supplied the pressure-ratio and efficiency entries in Table 3. Pressure-ratio changes were - 0.03 % to - 0.42 %, and the absolute isentropic-efficiency decreases were 0.16 – 0.79 percentage points for G1 – G7. G7 decreased efficiency from 84.62 % to 84.04 %, an absolute decrease of 0.58 percentage points and a relative decrease of 0.69 %; both the definition and the 0.80 threshold are reported in percentage points throughout. Passage-flow inspection found no additional separation at the shroud and only a 0.6 % rise in trailing-edge entropy generation.

At the design flow coefficient, G0 and G7 total pressure ratios were 2.184 and 2.175, while isentropic efficiencies were 84.62 % and 84.04 %. At 80 % and 120 % design flow, the maximum efficiency deficit remained 0.72 %, and the stable flow range contracted by less than 0.5 percentage points. Tip Mach number changed by only 0.003 because the aerodynamic surfaces were held fixed and thickness was redistributed mainly normal to the camber surface. Blade-passing pressure pulsation at the diffuser inlet rose 2.1 %, still below the structural reduction in synchronous response. The lack of a large flow penalty is important:

an efficiency-neutral thickness change can be judged primarily on mass and reliability, whereas a modified camber or exit angle would require a different multi-physics balance. The present constraint strategy therefore preserved interpretability as well as performance.

(3) Thermo-mechanical response and optical validation

At 900 °C and 60 krpm, the peak G0 principal tensile stress was 306.8 MPa at the blade-root/backplate junction, whereas G7 reached 266.5 MPa, a 13.14 % reduction (Table 3). **Fig. 3C** shows that G7 broadened the load-transfer path and displaced the maximum away from the free-surface fillet. Maximum deformation fell from 72.4 to 59.6 μm (17.68 %). The mass decrease reduced centrifugal force, while the thicker root decreased the local structural compliance; these two mechanisms acted in the same direction. Fluid-structure analyses of ultra-high-speed pump rotors have likewise identified bearing location and impeller transition stiffness as dominant contributors to deformation and stress [28]. Across mesh refinements, the stress change was 0.7 % and displacement change was 0.5 %, both smaller than the G0 – G7 differences.

Load decomposition clarified the coupled mechanism. With centrifugal loading alone, G7 reduced peak stress by 10.1 %; with the mapped temperature field alone, it reduced stress by 7.3 %; applying both fields produced the 13.1 % net reduction rather than the arithmetic sum because the thermal and rotational principal directions were not coincident. The maximum metal-to-ceramic interface temperature remained below 214 °C due to the cooled bearing region, while the blade tip reached 881 °C. G7 increased neither the peak temperature nor the hub gradient by more than 3 °C. A ± 15 % heat-transfer perturbation changed absolute peak stress by up to 12.8 MPa but changed the G7 – G0 contrast by only 2.3 MPa. Similarly, the lower 95 % conductivity bound moved the hotspot slightly toward the pressure side without returning it to the G0 root-filleting pattern. The structural advantage was therefore not contingent on one thermal boundary estimate.

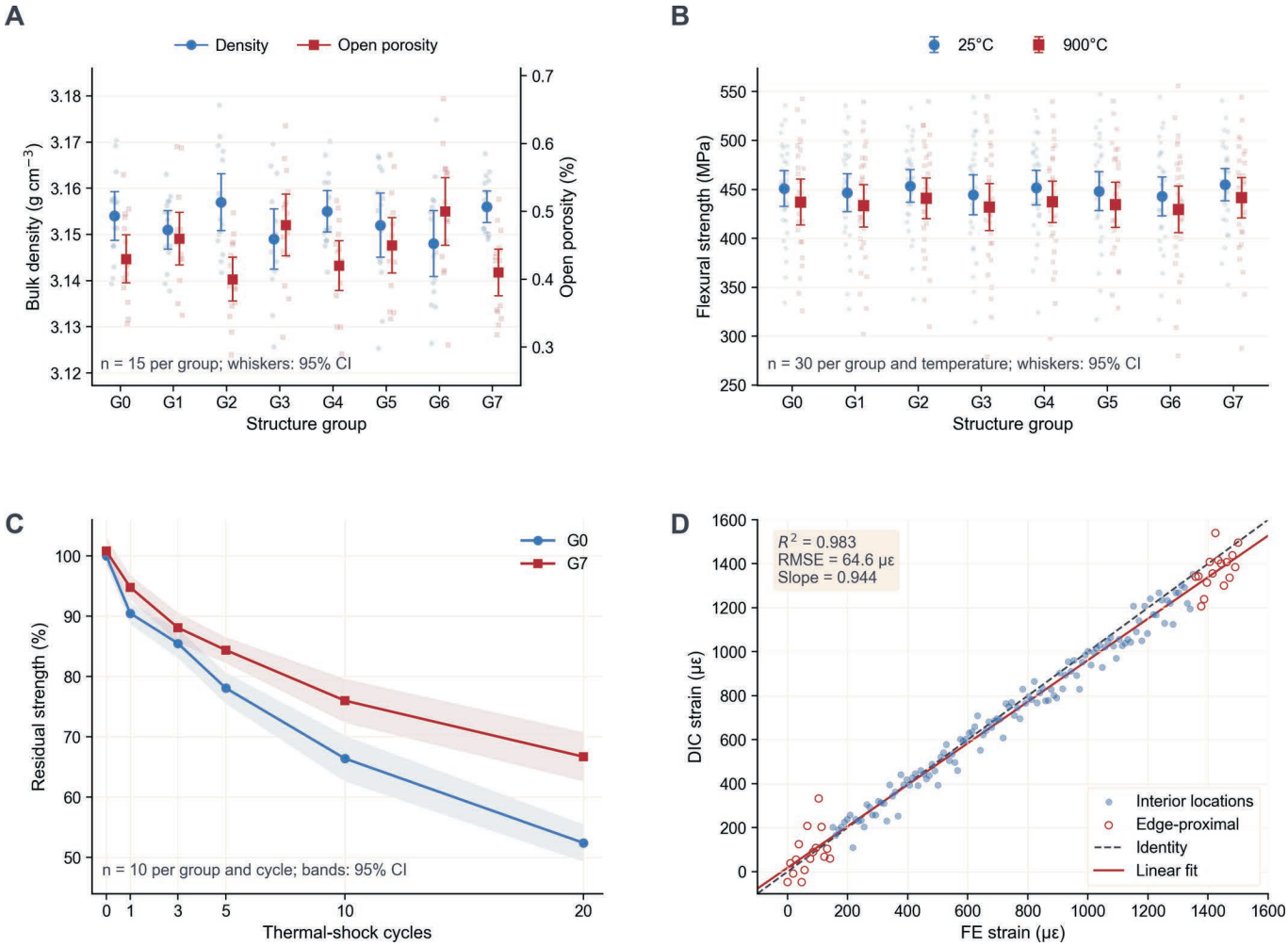


Fig. 4: Material and thermo-mechanical verification. (A) Bulk density and open porosity for 15 independent specimens per group; bars show means and whiskers show 95 % confidence intervals. (B) Flexural strength at 25 and 900 °C for 30 independent bars per group and temperature. (C) Residual strength of G0 and G7 after 0 – 20 thermal-shock cycles. (D) DIC strain versus finite-element strain at 160 paired technical locations nested within 16 impellers; the dashed line denotes identity and the inset reports R^2 and RMSE.

The replicated property measurements in **Fig. 4A** first show that bulk density (3.148 – 3.157 g cm^{-3}) and open porosity (0.40 – 0.50 %) remained tightly grouped across G0 – G7, with overlapping 95 % confidence intervals. **Fig. 4B** then shows comparable flexural-strength distributions at 25 and 900 °C. The 25 °C omnibus comparison was nonsignificant (p = 0.979), the batch-adjusted 900 °C analysis gave the same conclusion, and the maximum G0 – G7 difference in intrinsic strength was below 1.0 %. Together, these panels confirm that the component-level response was not produced by selective material strengthening.

Thermal-shock retention provided a deliberately discriminating component-level proxy. **Fig. 4C** shows that, after 20 cycles, G0 retained 52.4 ± 4.3 % of initial strength, whereas G7 retained 66.7 ± 5.7 %. The adjusted difference was 14.3 percentage points (95 % CI 9.5 – 19.0; Holm-adjusted $p < 0.001$; Hedges' $g = 2.72$). The wider late-cycle bands reflect accumulated crack-path variability rather than uniform degradation. The improved G7 retention arose despite equivalent coupon properties because its root transition reduced the tensile gradient produced during quenching. Each plotted cycle mean represented ten bars distributed across all three batches.

Fig. 4D provides a full-field technical comparison rather than 160 independent replicates. The 160 paired locations were nested within 16 impellers, and inference used the impeller as the experimental unit. Across locations, DIC and finite-element strain gave $R^2 = 0.983$, RMSE = 65 μstrain, mean bias = - 24 μstrain, and 95 % limits of agreement from - 142 to 93 μstrain. The fitted slope of 0.944 indicates modest high-strain under-response. Locations were retained to evaluate spatial agreement, whereas confidence intervals and hypothesis tests were based on specimen-level summaries or clustered models.

Repeatability across batches was acceptable rather than exact. The within-impeller DIC coefficient of variation at the root was 5.7 % for G0 and 6.3 % for G7, while between-batch variation was 3.8 % and 4.4 %, respectively. Removing the 32 most edge-proximal locations changed R^2 from 0.983 to 0.976 and RMSE from 65 to 60 μstrain, indicating that random measurement scatter was distributed through the field rather than confined to a few convenient outliers. At 600 °C the G7-to-G0 root-strain ratio was 0.88, and at 900 °C it was 0.86, closely tracking the stress-field ratio. This temperature consistency supports using the calculated field, with propagated optical uncertainty, rather than a sparse gauge maximum in the subsequent volume reliability integral.

Maximum-likelihood Weibull moduli at 25 °C ranged from 9.7 to 12.5 and overlapped broadly among groups; G0 was 11.22 (95 % bootstrap CI 8.58 – 16.50). At 900 °C, G0 was 8.58 (6.99 – 12.33), showing the expected increase in scatter under thermal loading. Deviations from a single flaw population were checked with probability plots and leave-one-out fits because ceramic data can depart from a straight Weibull line when several defect classes compete [29]. No group showed a reproducible kink, and three-parameter fits produced unstable thresholds. The two-parameter form was therefore retained, consistent with the weakest-link distribution originally proposed for brittle failure [30]. Maximum-likelihood estimates were used instead of regression on ranked probabilities to limit small-sample bias [31].

Brown-Forsythe tests supported equal variance for flexure ($F = 0.859$, $p = 0.540$), whereas the repeated vibration data were heteroscedastic across speed. Robust variance testing was chosen because it is less sensitive to nonnormal strength tails than a mean-centered Levene statistic [32]. Welch procedures were used for the vibration endpoint, following the unequal-variance logic of the alternative mean comparison [33]. Where pairwise comparisons were required, Games-Howell intervals were used rather than pooled-error contrasts [34]. These choices matter because an apparently precise structural improvement can otherwise be created by ignoring the higher dispersion near a critical speed.

(4) Rotor dynamics, vibration, and overspeed behavior

The Campbell map in **Fig. 5A** shows that G0 crossed the second forward mode at 62.1 krpm, only 3.5 % above the continuous 60 krpm limit, whereas G7 shifted that crossing to 69.0 krpm and increased separation margin to 15.0 % (Table 3). First critical speed also increased from 22.4 to 24.4 krpm. The change is physically consistent with a lower polar mass moment combined with greater root stiffness. Foundation-aware and rotor-stator-interaction studies warn that support dynamics can shift apparent crossings even when the rotor geometry is unchanged [35,36]. Bearing coefficients were therefore perturbed by ±10 %; the G7 second critical speed remained 6.1 – 7.6 krpm above G0 in every sensitivity case. Damping ratio rose from 1.18 % to 1.58 %, further suppressing the resonance response.

Coast-up and coast-down crossings differed by 0.42 krpm for G0 and 0.31 krpm for G7, values consistent with mild temperature lag rather than nonlinear jump behavior. The first mode was shaft-dominated and moved little among candidates, whereas the second mode combined shaft bending with impeller umbrella deformation and was therefore sensitive to blade mass distribution. Modal assurance criterion values between calculated and LDV shapes were 0.94 for G0 and 0.96 for G7. Cross-orthogonality remained above 0.90 after mass normalization. A 0.30 g·mm residual imbalance changed resonance amplitude but shifted critical speed by less than 0.15 krpm. These checks separate frequency placement from excitation magnitude: G7 improved both, but the higher separation margin derives from stiffness and inertia, while the lower observed peak also benefits from the measured damping increase.

The speed-frequency waterfall in **Fig. 5B** contained a broad first-bending ridge and a sharper second-mode ridge near the G0 crossing. At 900 °C/60 krpm, means were 3.44 ± 0.48 mm s^{-1} for G0 and 2.28 ± 0.60 mm s^{-1} for G7, a 33.7 % reduction with appreciable rotor-to-rotor overlap. The full batch-aware mixed model included 1 008 observations from 48 impellers; the prespecified G0 – G7 coefficient model included 252 observations from 12 impellers. The G7-by-speed estimate was - 0.229 mm s^{-1} per 10 krpm (SE 0.043; Kenward-Roger df = 10.8; 95 %

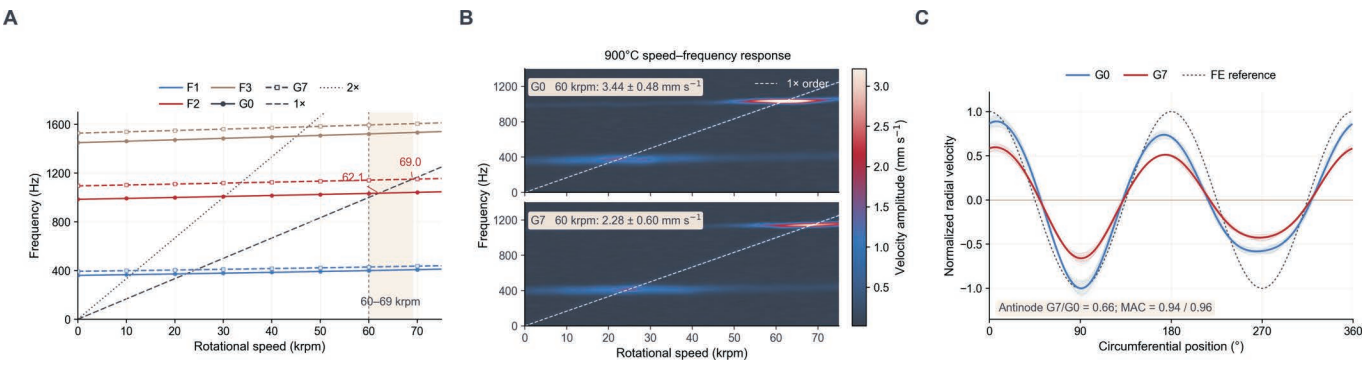


Fig. 5: Rotor-dynamic response. (A) Campbell map with the first three forward modes, 1× and 2× excitation lines, and the 60–69 krpm separation region. (B) Speed-frequency waterfall of vibration velocity, in which the broad first-bending ridge and localized second-mode ridge are resolved. (C) Laser-Doppler-vibrometry operating deflection shapes for G0 and G7 at 900 °C and 60 krpm, normalized to the G0 antinode. Dynamic tests used six impellers per group from three independent batches.

CI - 0.325 to - 0.133; Holm-adjusted p < 0.001). Batch, rotor, speed-slope, and residual variances were 0.012, 0.038, 0.0032, and 0.0625, respectively, and residual AR(1) correlation was 0.41. Marginal R^2 was 0.780 and conditional R^2 was 0.797. The design-by-temperature terms were nonsignificant, and both three-way intervals crossed zero, indicating that G7 primarily changed speed sensitivity rather than the shared temperature trend.

Temperature increased vibration gradually at a fixed subcritical speed, but the increment accelerated near the second-mode ridge. From 25 to 900 °C, G0 RMS rose 18.6 % at 40 krpm and 24.3 % at 60 krpm; corresponding G7 changes were 17.9 % and 21.1 %. The mixed model's nonsignificant optimized-by-temperature coefficient indicates that both designs shared the same thermal trend, whereas the significant optimized-by-speed coefficient captures a growing benefit with speed. The three-way interaction was small and its 95 % interval crossed zero. Batch-centered refitting, log-response fitting, and generalized estimating equations all preserved the negative design-by-speed direction. This convergence across link and covariance assumptions is more informative than one *p* value, especially because repeated speed points within an impeller are strongly correlated. The residual autocorrelation after random-slope fitting fell below 0.12 at every lag.

The confirmatory 900 °C/60 krpm Welch contrast remained significant after Holm correction (adjusted p = 0.0266), but its uncertainty was no longer negligible: Welch t = 3.71, Hedges' g = -1.98, and the 95 % bootstrap interval for g was −4.52 to −1.04. Achieved power was 0.87. Residual Q-Q plots showed mild tail compression without a systematic S-shape, and deleting the two largest residuals changed the G7 – G0 mean difference by less than 7 %. Marginal and conditional R^2 were reported separately because fixed design effects and clustered rotor-to-rotor variability answer different questions [37]. The nonzero batch and rotor components prevented pseudo-replication across the two impellers sampled from each batch.

Fig. 5C shows that the G0 and G7 operating deflection shapes retained the same two-lobed bending family, while G7 reduced normalized antinode amplitude by 34 %. Noncontact measurement was important because a bonded accelerometer would represent a non-negligible local mass on the thin ceramic tip. The broad LDV literature identifies optical access, scan-coordinate correction, and speckle return as primary uncertainty sources for rotating surfaces [38]. Frequency-locked full-field methods can recover higher spatial resolution from ordinary-rate cameras when the vibration frequency is known [39]. A fixed-beam check at the shroud differed from the scanning result by 3.2 %, within the calibration interval reported for rotating-body LDV approaches [40]. Contemporary tracking measurements on bladed disks further support explicit correction for surface motion during continuous scans [41].

All six G7 impellers completed the 72 krpm, 900 °C, 10 min hold. Five of six G0 impellers completed the hold; one triggered the vibration shutdown without visible fragmentation. Peak RMS velocity was 5.14 ± 0.40 mm s^{-1} for G0 and 3.46 ± 0.46 mm s^{-1} for G7. The representative micro-CT slices in **Fig. 6A** show red segmented crack paths extending farther around the G0 blade-root/backplate transition than in the G7 optimum. These slices provide qualitative spatial context, whereas crack-volume fractions were calculated from the calibrated three-dimensional source volumes for six G0 and six G7 impellers and were 0.032 ± 0.016 % and 0.019 ± 0.007 %, respectively. The overlapping ranges and single shutdown require descriptive interpretation rather than a binary safety claim.

(5) Reliability synthesis and engineering implication

Effective-volume integration combined local tensile stress with common pooled 900 °C Weibull parameters because material equivalence was supported across geometries. The two-parameter inputs were modulus m = 9.06, scale strength σ_0 = 466.2 MPa, and flexure-reference effective volume V_0 = 118.6 mm^3. At each structural integration point, only the positive maximum principal stress contributed: $P(\text{failure}) = 1 - \exp\{-\Sigma_i[(w_i V_i/V_0)\{\max(\sigma_{1,i}, 0)/\sigma_0\}^m]\}$. Compressive principal stresses were assigned zero hazard, and the four-point Gauss rule of each quadratic tetrahedral element supplied $w_i V_i$. At 900 °C and 60 krpm, predicted P(failure) was 2.1×10^{-3} for G0 and 1.8×10^{-4} for G7. The paired temperature-speed domains in **Fig. 6B** extend this duty-point comparison across the studied operating envelope:

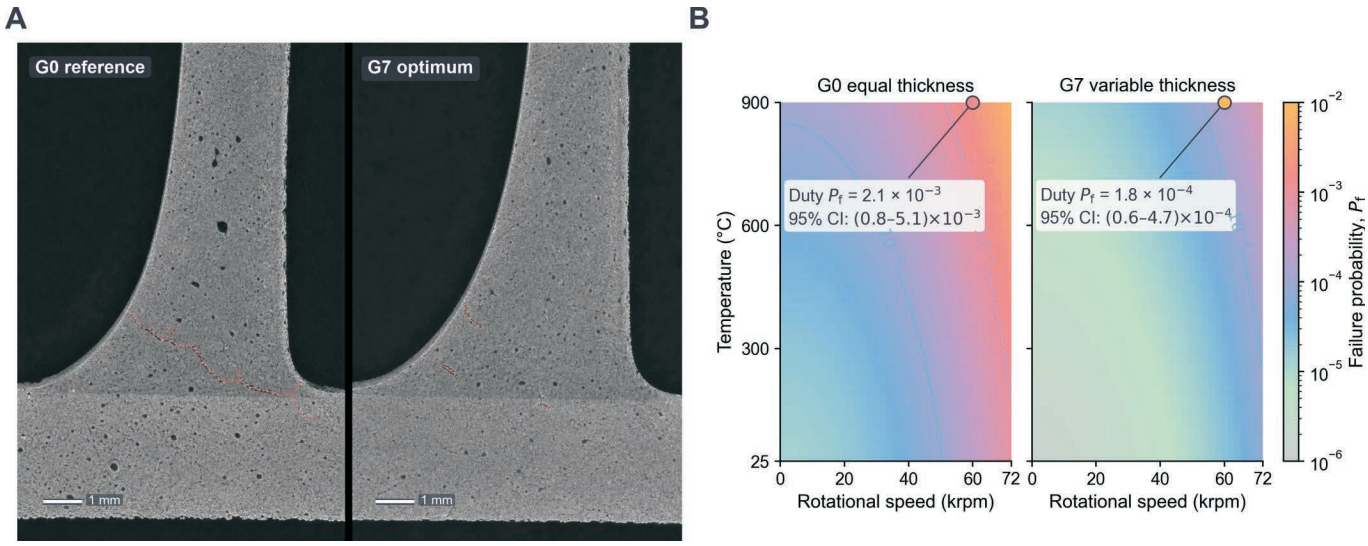


Fig. 6: Damage-informed reliability. (A) Micro-computed-tomography slice with the segmented crack path in red and the G7 mean ± SD crack-volume fraction. (B) Temperature-speed failure-probability domain with P_f iso-probability contours.

the G0 field enters higher failure-probability bands more rapidly as rotational speed and temperature rise, whereas the corresponding G7 contours are displaced toward higher combined loading. The marked duty points therefore retain the same reliability ranking as the full-domain comparison.

The stressed-volume distribution makes this distinction explicit. G0 contained 214 mm³ above 250 MPa and 37 mm³ above 290 MPa; G7 contained 103 mm³ above 250 MPa and no integration-point volume above 290 MPa after mesh-volume averaging. A 2 000-sample joint bootstrap resampled bars within batch and retained paired strength/property vectors, thereby preserving empirical within-batch correlations; numerical mesh and bearing terms were drawn conditionally from their replicated covariance estimates. The resulting 95 % intervals were $0.8 – 5.1 \times 10^{-3}$ for G0 and $0.6 – 4.7 \times 10^{-4}$ for G7. Group-specific Weibull sensitivity fits changed absolute probabilities but did not reverse the ranking.

The reliability result remained directional under conservative alternatives. Reducing the 900 °C Weibull modulus by its lower bootstrap bound raised both absolute probabilities, but G7 retained at least a 6.4-fold advantage. Increasing bearing compliance by 10 %, thermal-contact resistance by 20 %, or gas-side heat-transfer coefficient by 15 % did not reverse the ranking. The exploratory association between open porosity and conductivity was weak after Benjamini-Hochberg correction, so no post hoc material covariate was used to improve the structural model [42]. Holm-adjusted confirmatory tests protected the limited set of predeclared G0 – G7 contrasts without applying an unnecessarily severe correction to every characterization endpoint [43]. Extreme-value reasoning further supports emphasis on the upper stress tail instead of the spatial mean [44].

The 72 krpm exposure supplied a deliberately severe, short-duration challenge rather than a lifetime estimate. The one G0 shutdown occurred at a velocity threshold before fragmentation, and its CT crack fraction was the largest in that group. Treating the shutdown as a failure produced a risk ratio favoring G7, but the interval was wide because only twelve impellers entered the test; this endpoint was therefore interpreted descriptively. More persuasive is the agreement between three independent indicators: predicted risk, measured vibration, and post-run crack volume all favored G7. Spearman correlation between peak overspeed velocity and crack volume was 0.71, with a Benjamini-Hochberg-adjusted q below 0.05. Removing the shutdown rotor reduced the correlation to 0.63 but preserved its direction. This pattern supports, without overstating, a link from dynamic amplification to localized ceramic damage.

Taken together, the data identify G7 as a balanced rather than absolute optimum. G6 was lighter by 6.4 g, but its lower critical-speed margin and higher predicted risk outweighed that 2.8 % mass advantage. G7 achieved a 19 % mass reduction, 13 % stress reduction, 18 % deformation reduction, 11 % rise in second critical speed, and one-order reliability improvement while keeping efficiency loss to 0.58 %. The causal chain is internally consistent across independent modalities: the thickness curve redistributes stiffness; the stress field and DIC show lower root strain; the Campbell map and LDV show reduced dynamic amplification; and micro-CT shows less connected damage after overspeed. Because intrinsic properties remained nearly constant, this chain is attributable to structure rather than a hidden material change. The principal limitation is that long-duration oxidation, foreign-object impact, and bearing degradation were outside the present duty cycle. Those factors should be incorporated before certification, but they do not negate the demonstrated design mechanism.

IV. Conclusions

A variable-thickness pressureless-sintered SiC impeller was optimized and evaluated against an equal-thickness baseline and six intermediate candidates. The balanced G7 geometry placed additional material at the blade root

and backplate transition while thinning the mid-span and tip. This redistribution lowered mass from 286.4 to 232.1 g, reduced 900 °C/60 krpm principal tensile stress from 306.8 to 266.5 MPa, and reduced maximum deformation from 72.4 to 59.6 μm. Direct CFD showed an absolute efficiency decrease of 0.58 percentage points (0.69 % relative), below the robust 0.80 percentage-point constraint.

Material characterization showed comparable SiC phase fractions, density, porosity, grain size, flexural strength, fracture toughness, thermal conductivity, and expansion coefficient across all eight structures. The shared material response and nonsignificant strength differences isolated geometry as the main cause of component-level improvement. DIC and finite-element strain retained strong but imperfect agreement ($R^2 = 0.983$; RMSE = 65 μstrain), while replicated thermal-shock tests showed 66.7 ± 5.7 % residual strength for G7 versus 52.4 ± 4.3% for G0 after 20 cycles.

Rotor-dynamic measurements confirmed that the second critical speed increased from 62.1 to 69.0 krpm, separation margin increased from 3.5 % to 15.0 %, and 900 °C/60 krpm vibration RMS decreased from 3.44 ± 0.48 to 2.28 ± 0.60 mm s^{-1}. All G7 rotors completed the 72 krpm hold, compared with five of six G0 rotors, and the two crack-volume distributions overlapped despite a lower G7 mean. Maximum-likelihood Weibull analysis with effective-volume integration reduced the predicted duty-point failure probability from 2.1×10^{-3} (95 % CI $0.8 – 5.1 \times 10^{-3}$) to 1.8×10^{-4} ($0.6 – 4.7 \times 10^{-4}$).

The combined evidence supports continuous thickness redistribution as a practical route to lighter and more stable ceramic rotors. The key design lesson is that minimum mass alone is insufficient: local root stiffness, highly stressed volume, aerodynamic loss, and modal separation must be optimized together. Future qualification should add long-duration oxidation, foreign-object impact, shaft-joint degradation, and probabilistic bearing aging, while preserving batch replication and full-field validation. Scale-up should also verify machining tolerances at the thin tip and transfer the Weibull integral to production-specific flaw populations. Within the studied envelope, however, G7 provides the most favorable and statistically supported balance of mass, thermomechanical integrity, vibration control, and reliability.

Acknowledgements

This work was supported by the Project of Nanjing Agricultural Robot and Equipment Engineering Research Center (Grant no. [2024] 643).

References

1 Khodaei, M., Yaghobizadeh, O., Naghavi Alhosseini, S.H., Esmaeeli, S., Mousavi, S.R.: The effect of oxide, carbide, nitride and boride additives on properties of pressureless sintered SiC: A review, *J. Eur. Ceram. Soc.*, **39**, 2215 – 2231, (2019).

2 Seo, Y.-K., Eom, J.-H., Kim, Y.-W.: Process-tolerant pressureless-sintered silicon carbide ceramics with alumina-yttria-calcia-strontia, *J. Eur. Ceram. Soc.*, **38**, 445 – 452, (2018).

3 Xu, T.-T., Cheng, S., Jin, L.-Z., Zhang, K., Zeng, T.: High-temperature flexural strength of SiC ceramics prepared by additive manufacturing, *Int. J. Appl. Ceram. Technol.*, **17**, 438 – 448, (2020).

4 Takeda, Y., Maeda, K.: Thermal shock resistance of high thermal conductive SiC ceramics, *J. Ceram. Soc. Jpn.*, **99**, 1153 – 1155, (1991).

5 Lamon, J.: Investigation of variability of flaw strength distributions on brittle SiC ceramic, *Ceramics*, **7**, 759 – 776, (2024).

6 Takeo, K., Aoki, Y., Osada, T., Nakao, W., Ozaki, S.: Finite element analysis of the size effect on ceramic strength, *Materials*, **12**, 2885, (2019).

7 Zinszner, J.-L., Erzar, B., Forquin, P.: Strain rate sensitivity of the tensile strength of two silicon carbides: experimental evidence and micromechanical modelling, *Philos. Trans. R. Soc. A*, **375**, 20160167, (2017).

8 Padovano, E., Badini, C., Mergia, K., Barcena, J.: Thermophysical and radiative properties of pressureless sintered SiC and ZrB_2-SiC laminates, *Ceram. Int.*, **44**, 15050 – 15057, (2018).

9 Nakashima, S.-I., Higashihira, M., Maeda, K., Tanaka, H.: Raman scattering characterization of polytype in silicon carbide ceramics: comparison with X-ray diffraction, *J. Am. Ceram. Soc.*, **86**, 823 – 829, (2003).

10 Li, Z., Bradt, R.C.: Thermal expansion of the hexagonal (6H) polytype of silicon carbide, *J. Am. Ceram. Soc.*, **69**, 863 – 866, (1986).

11 Datta, M.S., Bandyopadhyay, A.K., Chaudhuri, B.: Strength and microstructure of sintered alpha-silicon carbide prepared from nano-crystalline particles doped with boron carbide, *Trans. Indian Ceram. Soc.*, **61**, 75 – 79, (2002).

12 McKay, M.D., Beckman, R.J., Conover, W.J.: A comparison of three methods for selecting values of input variables in the analysis of output from a computer code, *Technometrics*, **21**, 239 – 245, (1979).

13 Deb, K., Pratap, A., Agarwal, S., Meyarivan, T.: A fast and elitist multiobjective genetic algorithm: NSGA-II, *IEEE Trans. Evol. Comput.*, **6**, 182 – 197, (2002).

14 Rasmussen, C. E., Williams, C.K.I.: Gaussian Processes for Machine Learning. 1st ed., MIT Press, Cambridge, MA, (2006).

15 Palar, P. S., Shimoyama, K.: On efficient global optimization via universal kriging surrogate models, *Struct. Multidiscip. Optim.*, **57**, 2377 – 2397, (2018).

16 Rietveld, H.M.: A profile refinement method for nuclear and magnetic structures, *J. Appl. Crystallogr.*, **2**, 65 – 71, (1969).

17 Kaczmarek, R., Dupre, J.-C., Doumalin, P., Pop, O., Teixeira, L., Huger, M.: High-temperature digital image correlation techniques for full-field strain and crack length measurement on ceramics at 1200 degrees C, *Opt. Lasers Eng.*, **146**, 106716, (2021).

18 Bumgardner, C., Croom, B., Li, X.: High-temperature delamination mechanisms of thermal barrier coatings: In-situ digital image correlation and finite element analyses, *Acta Mater.*, **128**, 54 – 63, (2017).

19 Sheng, Z., Chen, B., Hu, W., Yan, K., Miao, H., Zhang, Q., Yu, Q., Fu, Y.: LDV-induced stroboscopic digital image correlation for high spatial resolution vibration measurement, *Opt. Express*, **29**, 28134 – 28147, (2021).

20 Liu, C., Xu, T., Chen, T., Su, S., Huang, J., Li, Y.: Operational deflection shape measurements on bladed disks with continuous scanning laser doppler vibrometry, *Sensors*, **24**, 3413, (2024).

21 Liu, S., Liu, F., Zhang, Q., Li, Z., Zhang, B., Wang, L.: Non-destructive characterisation and evaluation of manufacturing defects in SiCf/SiC composites using the relative energy attenuation behaviour of X-rays, *Ceram. Int.*, **46**, 26044 – 26054, (2020).

[22] Magnani, G., Beltrami, G., Minoccari, G. L., Pilotti, L., Scafe, E., Brentari, F.: Pressureless sintering and properties of alpha-SiC-B_4C composite, *J. Eur. Ceram. Soc.*, **21**, 633 – 638, (2001).

[23] Malik, R., Kim, Y.-H., Kim, Y.-W.: Effect of additive content on the mechanical and thermal properties of pressureless liquid-phase sintered SiC, *J. Asian Ceram. Soc.*, **8**, 448 – 459, (2020).

[24] Li, X., Zhang, K., Konietzky, H., Wang, Y., Li, X.: Experimental study on the dynamic mechanical behaviors of silicon carbide ceramic after thermal shock, *Nucl. Mater. Energy*, **24**, 100774, (2020).

[25] Kim, J.-H., Choi, J.-H., Husain, A., Kim, K.-Y.: Multi-objective optimization of a centrifugal compressor impeller through evolutionary algorithms, *Proc. Inst. Mech. Eng. Part A J. Power Energy*, **224**, 711 – 721, (2010).

[26] Xie, X., Li, Z., Zhu, B., Wang, H.: Multi-objective optimization design of a centrifugal impeller considering both aerodynamic efficiency and structural machinability, *Eng. Comput.*, **38**, 2755 – 2780, (2021).

[27] Wu, T., Wu, D., Gao, S., Song, Y., Ren, Y., Mou, J.: Multi-objective optimization and loss analysis of multistage centrifugal pumps, *Energy*, **284**, 128638, (2023).

[28] Yan, S., Ye, Z., Wang, D., Ma, J., Zhou, W.: Structural analysis and optimization of ultra-high-speed centrifugal pump rotor system considering fluid-structure interaction, *Water*, **16**, 1471, (2024).

[29] Danzer, R., Supancic, P., Pascual, J., Lube, T.: Fracture statistics of ceramics: weibull statistics and deviations from weibull statistics, *Eng. Fract. Mech.*, **74**, 2919 – 2932, (2007).

[30] Weibull, W.: A statistical distribution function of wide applicability, *J. Appl. Mech.*, **18**, 293 – 297, (1951).

[31] Quinn, G.D., Quinn, J.B.: A practical and systematic review of weibull statistics for reporting strengths of dental materials, *Dent. Mater.*, **26**, 135 – 147, (2010).

[32] Brown, M.B., Forsythe, A.B.: Robust tests for the equality of variances, *J. Am. Stat. Assoc.*, **69**, 364 – 367, (1974).

[33] Welch, B.L.: On the comparison of several mean values: an alternative approach, *Biometrika*, **38**, 330 – 336, (1951).

[34] Games, P.A., Howell, J.F.: Pairwise multiple comparison procedures with unequal n and/or variances, *J. Educ. Stat.*, **1**, 113 – 125, (1976).

[35] Hajzman, M., Balda, M., Polcar, P., Polach, P.: Turbine rotor dynamics models considering foundation and stator effects, *Machines*, **10**, 77, (2022).

[36] Olimstad, G., Ostby, P.T.K.: Failure and redesign of a high-speed pump with respect to rotor-stator interaction, *Eng. Fail. Anal.*, **104**, 704 – 713, (2019).

[37] Nakagawa, S., Schielzeth, H.: A general and simple method for obtaining R^2 from generalized linear mixed-effects models, *Methods Ecol. Evol.*, **4**, 133 – 142, (2013).

[38] Rothberg, S.J., Allen, M.S., Castellini, P., *et al.*: An international review of laser doppler vibrometry: making light work of vibration measurement, *Opt. Lasers Eng.*, **99**, 11 – 22, (2017).

[39] Wang, P., Chen, B., Gao, Z., Fu, Y., Chen, S., Zhu, X.: High precision full-field vibration measurement by LDV-induced stroboscopic fringe projection, *Opt. Lasers Eng.*, **183**, 108481, (2024).

[40] Artelnyi, V.V., Rodionov, A.A., Stulenkov, A.V.: Increasing the frequency resolution when measuring vibrations of rotating bodies with fixed beam laser vibrometry, *Acoust. Phys.*, **69**, 367 – 371, (2023).

[41] Liu, C., Jing, T., Xu, Z., Liu, L., He, J.: Operational deflection shape measurements on rotating bladed disks with tracking continuous-scanning LDV, *Sci. Rep.*, **16**, 16495, (2026).

[42] Benjamini, Y., Hochberg, Y.: Controlling the false discovery rate: A practical and powerful approach to multiple testing, *J. R. Stat. Soc. B*, **57**, 289 – 300, (1995).

[43] Holm, S.: A simple sequentially rejective multiple test procedure, *Scand. J. Stat.*, **6**, 65 – 70, (1979).

[44] Fisher, R.A., Tippett, L.H.C.: Limiting forms of the frequency distribution of the largest or smallest member of a sample, *Math. Proc. Camb. Philos. Soc.*, **24**, 180 – 190, (1928).